Yttria-zirconia coatings studied by grazing-incidence small-angle X-ray scattering during in situ heating

Hoydalsvik, Kristin; Barnardo, Twilight; Winter, Rudolf; Haas, Sylvio; Tatchev, Dragomir; Hoell, Armin

Published in:
Physical Chemistry Chemical Physics

DOI:
10.1039/C0CP00472C

Publication date:
2010

Citation for published version (APA):
Hoydalsvik, K., Barnardo, T., Winter, R., Haas, S., Tatchev, D., & Hoell, A. (2010). Yttria-zirconia coatings studied by grazing-incidence small-angle X-ray scattering during in situ heating. *Physical Chemistry Chemical Physics*, *12*(43), 14492-14500. https://doi.org/10.1039/C0CP00472C

Yttria-zirconia coatings studied by grazing-incidence small-angle x-ray scattering during *in-situ* heating

Kristin Hoydalsvik,[a†] Twilight Barnardo,[a] Rudolf Winter,[*a] Sylvio Haas,[b] Dragomir Tatchev,[b‡] and Armin Hoell[b]

Received Xth XXXXXXXXXX 20XX, Accepted Xth XXXXXXXXX 20XX
First published on the web Xth XXXXXXXXXX 200X
DOI: 10.1039/b000000x

The morphology of sol-gel derived dip-coated yttria-doped zirconia films containing variable amounts of yttria has been studied using *in-situ* Grazing-Incidence Small-Angle X-ray Scattering (GISAXS) whilst heated incrementally to 1000°C.
A procedure to analyse *in-situ* GISAXS data has been devised which allows a quantitative analysis of time-dependent GISAXS data tracing processes such as chemical reactions or manufacturing procedures. To achieve this, the relative positions of the Yoneda peak and the through beam are used to fix the vertical q scale when the sample thickness is subject to fluctuations due to chemical reactions or deposition processes.
A version of Beaucage's unified model with a structure factor from Hosemann's model for paracrystals describes the yttria-zirconia film data best. It is interpreted in terms of particles forming from a polymeric gel network and subsequently agglomerating into larger units subject to Ostwald ripening as both size and average separation distance of the scattering objects increase. The sample with the highest yttria content shows progressive surface roughening from 850°C which may indicate the onset of chemical segregation.

1 Introduction

Films and coatings are used for many applications such as photovoltaic cells[1], influencing optical properties of glass[2], production of yttrium barium copper oxide (YBCO) superconductors[3], and for solid oxide fuel cells (SOFC)[4]. Zirconium dioxide thin films play an important role as high-k dielectrics and DRAM storage capacitors[5], and YSZ (yttria-stabilised zirconia) films show good proton and ionic conductivity[6,7] and oxygen transport[4]. YSZ coatings are also found to be a good thermal barrier material[8].

We have studied bulk YSZ using Anomalous Small-Angle X-ray Scattering (ASAXS) and found that pure zirconia crystals initially nucleate and absorb yttria as they grow, which results in stabilisation of the cubic phase[9].

Sol-gel processing is an effective way of manufacturing zirconia and yttria-stabilised zirconia thin films, and dip-coating is a controlled way of producing flat thin films from these sols. The thickness of the film can be controlled by varying the withdrawal speed, the viscosity, or the density of the sol[10].

Since many coatings are used under high temperature conditions, it is important to have a method of investigating how heat influences these coatings, such as formation of patterns in the film, cracking, crystallisation behaviour, and thermal stability. Here we have studied dip-coated films, which are heated up to 1000°C using a purpose-built furnace which can be installed directly on a synchrotron beamline.

The technique employed is Grazing-Incidence Small-Angle X-ray Scattering. GISAXS was introduced in 1989 by Joanna Levine[11], and is very well suited to study thin film structure and particles within the film, on the surface, or at interfaces. It is a surface sensitive, non-destructive reciprocal space technique, which has the advantage that there is a large number of scattering particles that contributes to the signal, and therefore better statistics are obtained than real space techniques can typically achieve.

GISAXS is rarely used for *in-situ* studies chemical reactions or other processes because the technique is very sensitive to macroscopic changes to the sample geometry such as thermal expansion or changes in density, which are difficult to control during an *in-situ* experiment. In this paper, we develop a procedure for analysing *in-situ* GISAXS data quantitatively in the presence of such uncertainties based on the relative positions in the scattering patterns of the Yoneda peak and the through beam skimming the sample surface. This study investigates how yttria-doped zirconia coatings sinter as the temperature is increased, as an example of a quantitative *in-situ* GISAXS

[a] *Materials Physics, Aberystwyth University, Penglais, Aberystwyth SY23 3BZ, Wales. E-mail: ruw@aber.ac.uk*
[b] *Institute of Applied Materials, Helmholtz-Zentrum Berlin, Albert-Einstein-Strasse 15, 12489 Berlin, Germany*
[†] *Present address: Department of Physics, Norwegian University of Science and Technology, Høgskoleringen 5, 7491 Trondheim, Norway*
[‡] *Rostislaw Kaischew Institute of Physical Chemistry, Bulgarian Academy of Sciences, Sofia, Bulgaria*

experiment.

2 Theoretical background

The refractive index for x-rays is given by $n = 1 - \delta - i\beta$ (see, for example, Ref. [12]), where the real part, $1-\delta$, is characteristic for refraction, and the imaginary part, β, is characteristic for absorption [13]. Since the film is a compound material, δ and β are calculated using [14]

$$\delta = A'\rho\lambda^2 \frac{\sum_i n_i(Z_i + f_i')}{\sum_i n_i A_i} \quad \text{and} \quad \beta = A'\rho\lambda^2 \frac{\sum_i n_i f_i''}{\sum_i n_i A_i}, \qquad (1)$$

where ρ is the mass density of the film, λ is the wavelength of the incoming x-rays, n_i is the molar amount of constituent element i (from Tab.1), Z_i and A_i is the atomic number and mass, respectively, and f_i' and f_i'' are the anomalous correction factors to the atomic scattering factor. $A' = (N_A r_e)/(2\pi)$ where N_A is Avogadro's number and r_e is the classical electron radius.

The critical angle for total external reflection is found to be [12]

$$\alpha_c = \sqrt{2\delta}. \qquad (2)$$

2.1 Penetration depth

The refracted angle is found by using Snell's law (see, for example, Ref. [15]). The penetration depth Λ, where the beam intensity has fallen to 1/e of the incoming intensity, is calculated for the film in order to investigate the depth inside the film from which significant contributions to the scattered signal arise:

$$\Lambda = \frac{\lambda}{4\pi\Im(\alpha_1)}. \qquad (3)$$

$\Im(\alpha_1)$ is the imaginary part of the refracted angle in the film (see, for example, Ref. [15]).

The incoming beam is described by the wave vector $\mathbf{k}_i$ ($k_i = |\mathbf{k}_i| = 2\pi/\lambda$) at an angle α_i between it and the sample plane. The x-rays are scattered along $\mathbf{k}_f$ in the direction pointing along the angles ($2\theta_f$, α_f). The scattering vector $\mathbf{q} = (q_x, q_y, q_z)$ is defined by [16]

$$\mathbf{q} = \frac{2\pi}{\lambda} \begin{bmatrix} \cos(\alpha_f)\cos(2\theta_f) - \cos(\alpha_i) \\ \cos(\alpha_f)\sin(2\theta_f) \\ \sin(\alpha_f) + \sin(\alpha_i) \end{bmatrix}. \qquad (4)$$

For small and constant α_f, the following approximation is valid:

$$q_y \approx \frac{4\pi}{\lambda}\sin(\theta_f), \qquad (5)$$

which is recognised as the equation for the magnitude of the momentum transfer vector, q, for small-angle scattering in transmission setup (see, for example, Ref. [11]). The cuts taken parallel to the sample surface can therefore be treated as conventional SAXS patterns.

Yoneda discovered a surface reflection of x-rays at low angles [17] close to the critical angle,

$$\alpha_{Yoneda} \simeq \alpha_c. \qquad (6)$$

This feature is due to a fraction of the incoming beam which travels within the surface as an Evanescent wave and emerges at the far edge of the sample at the critical angle. Crucially for *in-situ* studies, the Yoneda peak depends only on the critical angle but is independent of the angle of incidence [18].

Table 1 Relative molar content ($n_{Zr} + n_Y + n_O = 1$) of the different samples.

Sample	n_{Zr}	n_Y	n_O	$\frac{n_{Y_2O_3}}{n_{Y_2O_3}+n_{ZrO_2}}$
	mol	mol	mol	mol%
A	0.328	0.007	0.666	1.01
B	0.322	0.014	0.664	2.09
C	0.280	0.065	0.656	10.3

3 Experimental

3.1 Sample preparation

The zirconia sol was prepared by mixing zirconium(IV)propoxide [$Zr(OCH_2CH_2CH_3)_4$], isopropanol [$(CH_3)_2CHOH$], acetylacetone ($CH_3COCH_2COCH_3$), acetic acid (CH_3COOH), and adding an isopropanol/water mixture (volume ratio 2:1). Yttria doping was obtained by grinding yttrium nitrate hexahydrate [$(Y(NO_3)_6 \cdot 6H_2O)$] by pestle and mortar and adding it to the isopropanol/water mixture before it was mixed with the main precursor solution. YSZ with different doping levels of yttrium-to-zirconium were prepared by adding varying amounts of yttrium nitrate corresponding to 1.01, 2.09 and 10.3 mol% Y_2O_3, as listed in Tab.1. These mixtures were called sample A, B, and C, respectively.

Silicon (100) wafers cut into rectangles of $\sim$(25 mm $\times$ 10 mm) were used as substrates. They were dip-coated with the appropriate sol using a withdrawal speed of 8.1 cm min^{-1}, and dried at 120°C for ten minutes. *Ex-situ* studies by ellipsometry showed that the film thickness decreases rapidly from initially $\sim$ 450 nm (after drying at 120°C) down to $\sim$ 100 nm at $T \geq 500$°C.

3.2 Experimental setup

The experiments were performed at the 7T-MPW-SAXS beamline at BESSY II, Berlin, using a MarCCD 165 detector [(2048 $\times$ 2048) pixels]. The x-ray energy was fixed to 10008 eV ($\lambda = 0.12389$ nm) during the entire experiment,

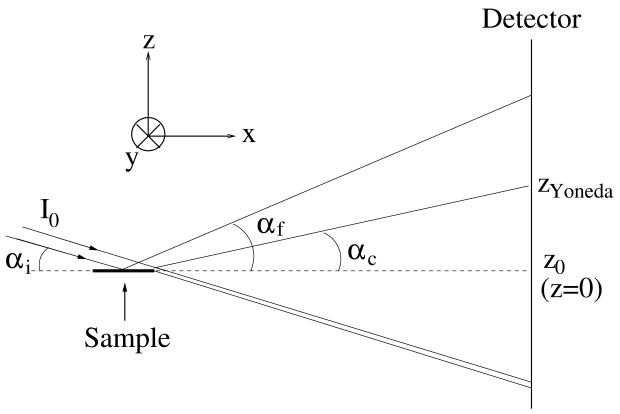

Fig. 1 Illustration of the sample geometry: The beam is incident at an angle α_i, and some of the beam misses the sample and hits the detector further down, while the rest of the beam is reflected and scattered from the sample with exit angles α_f (along the z-axis) and $2\theta_f$ (along the y-axis). The reflected specular beam is omitted in the figure. The sample surface plane is indicated at $z_0 = z(\alpha_f = 0)$, and the Yoneda feature is observed at $z_{Yoneda} = z(\alpha_f = \alpha_c)$. (The angles are exaggerated for clarity of illustration.)

which was set up as shown in Fig.1. Beamstops were used to block the strong specular reflection of the incident beam and the direct beam (the part of the beam that does not hit the sample and just continues in a straight line).

The sample surface lies in the $(x, y, z = 0)$ plane, the incident angle α_i and the exit angle α_f lie in the $(x, y = 0, z)$ plane, and the horizontal scattering angle $2\theta_f$ lies in the $(x, y, z = D\tan\alpha_f)$ plane, where D is the sample-detector distance.

Samples were heated using a purpose-built GISAXS furnace consisting of a circular hotplate 10 mm in diameter and a copper hood with replaceable Kapton windows. The hood is water-cooled, and it is possible to run with an inert atmosphere. The temperature is measured using a thermocouple wired into the heating element and can be controlled remotely since the experiment is located in a radiation hazard area. The sample was heated from 400°C, in steps of 50 degrees, up to 1000°C. The incident angle, α_i, was fixed to 0.257°. Ten individual measurements were taken for 30 seconds at each temperature step. This procedure was then repeated for different samples.

While the films as prepared are delicate, the coatings become stable following the heat treatment and bond well to the substrate. No flaking is observed when the coated surface is scratched with a pair of tweezers.

4 Results and discussion

4.1 A procedure for analysing *in-situ* GISAXS data

As shown in Fig.2, the GISAXS pattern changes significantly during heating runs. This occurs because the film structure changes as the temperature increases. At the same time, the density increases, which in turn causes δ and β to increase [see Eq. (1)]. According to Eq. (2), the critical angle for the film, α_c, will also increase, and consequently the Yoneda feature will be observed at higher exit angle α_f [Eq. (6)].

Consequently, horizontal cuts cannot simply be taken at fixed detector channels; instead a method is needed that finds the appropriate horizontal cut for each measurement such that the information obtained from each is comparable. A procedure to achieve this was developed and is described as follows.

The detector images were first normalised to measuring time and incoming beam current. The patterns typically change slightly during the first few measurements after ramping up the heating. Therefore, to allow for equilibration, the average of the last five of ten measurements in total was calculated at each temperature, and this result was used for further analysis. In order to improve statistics, each cut was averaged over four rows of pixels.

As an example, Fig.3 shows how the lines were selected for further 1D-SAXS analysis for sample B heated to 550°C. As indicated in (a), a vertical cut (b) was taken at the same horizontal pixel (width) value for the entire heating run since the setup of the sample does not change sideways (but the height may change because of thermal expansion). The main feature in (a) and (c) is the Yoneda feature, and the position of this peak (b) was used to determine where to make the horizontal cuts [(c) and (d)]. This procedure was repeated for each measurement.

The angular range for the horizontal cuts is $0.14° < 2\theta_f < 1.6°$, in both positive and negative direction, but only the positive $2\theta_f$- direction was used. The negative direction has a symmetrically equivalent pattern, but the area covered by the beamstop is not symmetric, hence only one of the sides was used. The point where $2\theta_f = 0$ was determined by finding the centre between equal intensities on the positive and negative sides. The horizontal cuts result in SAXS patterns that can be analysed further with conventional SAXS analysis methods [see Eq. (5)]. Some of the horizontal cuts are shown in Fig.4.

In order to scale the q_y axis of the horizontal cuts at z_{Yoneda}, the relation

$$q_y = \frac{4\pi}{\lambda}\sin(\theta_f), \quad \text{where} \quad 2\theta_f = \tan^{-1}\left(\frac{s(y-y_0)}{D}\right), \quad (7)$$

was used. $s = 79$ μm is the pixel size, $D = 2920$ mm is the sample-detector distance, y is the horizontal pixel coordinate

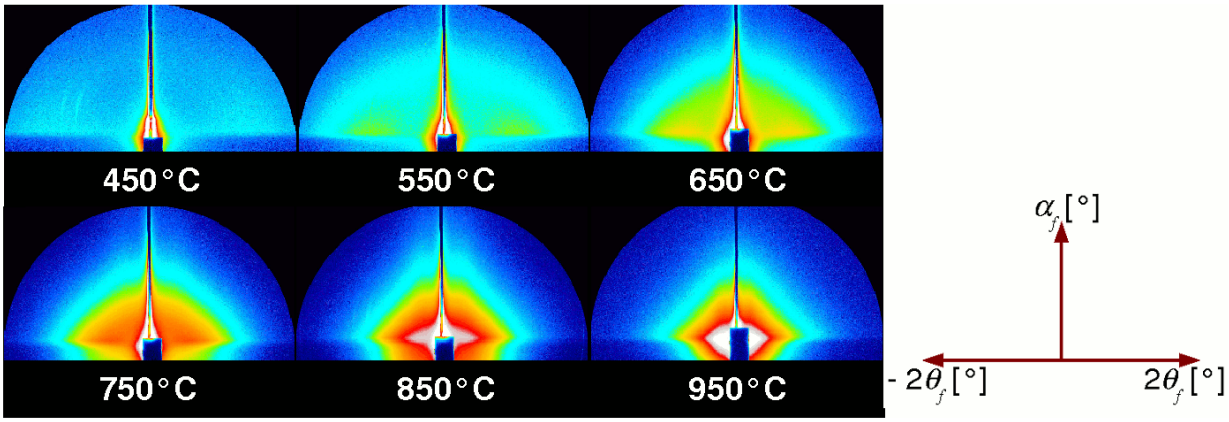

Fig. 2 The GISAXS patterns for sample B taken at different temperatures are shown to the left, and the axes labels are shown to the right. Note that the pattern changes significantly as the sample is heated; from having distinct wings, via more powder-like patterns, and finally broadening along the y- and z-directions. A method of extracting horizontal 1D cuts such that the different measurements are comparable was developed and is described in this section, and a suggested model of the sample development during heating is described in section 4.2.

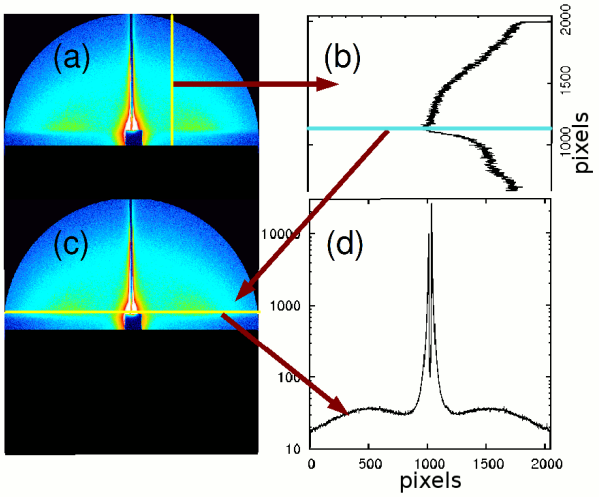

Fig. 3 Illustration of how the line was selected for further 1D analysis (Sample B, 550°C). A vertical line at a pixel number that was constant for all temperatures was selected (a). Then the 1D vertical cut was extracted, and the pixel number for the peak was found (b). This pixel number was used for finding the height at which to extract the 1D horizontal cut (c) shown in (d).

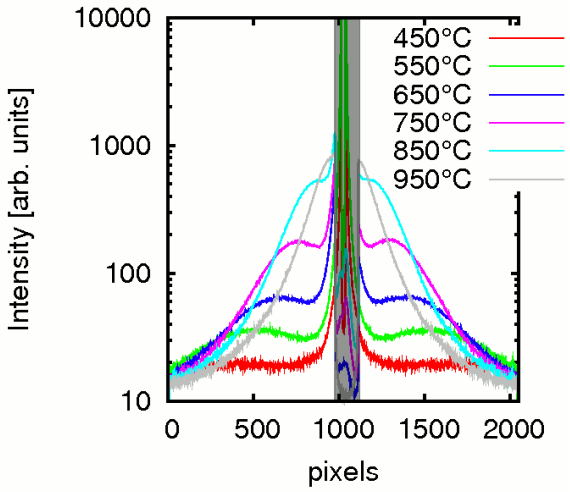

Fig. 4 1D horizontal cuts at the Yoneda feature for the different temperature measurements shown in Fig.2. The shaded area corresponds to the beamstop.

and y_0 is the horizontal position of the beam centre. This procedure was compared to measurements of the silver behenate calibrant (see, for example, Refs. [19,20]), and both methods gave the same result. For this experiment, the wave-vector range is $0.14\ \text{nm}^{-1} < q_y < 1.4\ \text{nm}^{-1}$.

The scaling for the vertical cuts was found by

$$\alpha_f(z) = \tan^{-1}\left(\frac{s(z-z_0)}{D}\right), \tag{8}$$

where α_f is the exit angle between the scattered beam and the film, z is the pixel number in the vertical direction, and z_0 is

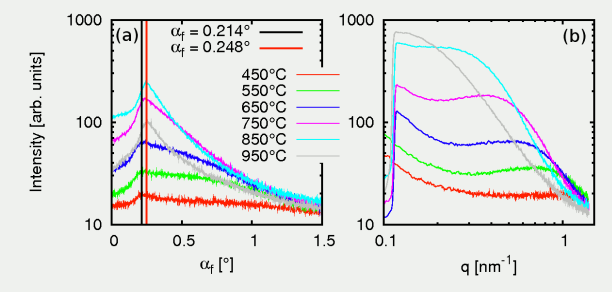

Fig. 5 Heating run for sample B (incident angle $\alpha_i = 0.257°$). (a) Vertical cuts taken as indicated in Fig.3(a). The peak is the Yoneda peak. (b) Horizontal cuts at the Yoneda feature, taken as indicated in Fig.3(c).

the sample plane (see Fig.1). z_0 was found by

$$z_0 = z_{Yoneda} - \frac{D}{s}\tan\alpha_c, \tag{9}$$

where z_{Yoneda} was found as shown in Fig.3, and α_c was calculated from Eqs. (1) and (2).

4.2 Sintering regimes depending on temperature

As the film is heated up, distinct wings are apparent for the medium temperatures (see Fig.2). For higher temperatures the scattering becomes more powder-like. At even higher temperatures, the scattering intensity is largest along the *y*- and *z*-directions.

1D cuts which are extracted from these 2D patterns using the procedure illustrated in Fig.3, are shown in Fig.5 for sample B. Fig.5(a) shows the vertical cuts for the line indicated in Fig.3(a) with the abscissa scaled after Eq. (8). Note that the peak position for the vertical cuts (Fig.5(a)), *i*.e. the Yoneda peak, shifts slightly, from $\alpha_f \approx 0.21°$ to $0.25°$ as the sample is heated, which corresponds to the density increase from $3750\,\mathrm{kg\,m^{-3}}$ to $5025\,\mathrm{kg\,m^{-3}}$ (Ref.[21]). Fig.5(b) shows the 1D horizontal cuts for the same measurements, at the cut indicated in Fig.3(c).

From the expressions for δ and β [Eq. (1)], it is clear that knowledge of the mass density of the material is rather critical to the further analysis. The mass density for the films increases as the sample is heated, and the relevant mass density for each temperature was found by comparing to previous experiments conducted by Lenormand *et al.*[21]. These authors prepared zirconia films using similar methods as we did, and measured thickness and mass density of the films as they were heated using x-ray reflectivity (XRR) measurements. Here it has been assumed that the mass densities obtained for the pure zirconia films can be used for the yttria-zirconia films, because the mass difference between yttrium and zirconium atoms is small. For example, the mass difference between crystalline zirconia and sample C (10.3 mol-% yttria) in crystalline form is less than 1%. For the uncalcined films it would be even smaller because the film densities are lower than the density of the crystalline material.

For example, for sample B heated to 1000°C the film density is then $\rho = 5150\,\mathrm{kg\,m^{-3}}$ (Ref.[21]). δ and β can now be calculated from Eq. (1) by setting $i = \{Zr\},\{Y\},\{O\}$ and n_i is taken from Tab.1. The anomalous correction factors, f' and f'', were found in Ref.[22] for $\lambda = 0.124$ nm; this is acceptable since the x-ray energy used here is far from any absorption edges. The results for this particular sample are found to be $\delta = 9.60\cdot10^{-6}$ and $\beta = 2.72\cdot10^{-7}$. The critical angle can now be found from Eq. (2), and for this sample it is $\alpha_c = 0.251°$. The film thickness was found from *ex-situ* ellipsometry measurements, and these showed that the thickness of this film was $t = 113 \pm 4$ nm. The calculations mentioned above were performed using Octave[23], and the source code can be found in Ref.[24].

During the heating experiment, the incident angle α_i was fixed to $0.257°$. As seen in Fig.2, the GISAXS patterns change from having distinct wings, via more powder-like patterns, and finally broadening along the *y*- and *z*-directions. The Yoneda feature moves slightly towards larger α_f as the sample is heated [see Fig.5(a)]. The critical angle for the heated films has been calculated using Eq. (2), and for example, $\alpha_c(450°\mathrm{C}) = 0.214°$ and $\alpha_c(950°\mathrm{C}) = 0.248°$.

These vertical cuts are taken at the same pixel value for all temperatures; far enough away from the central beamstop to be sure that it is the GISAXS signal that is measured rather than the diffuse intensity from the reflected beam, but at the same time close enough to obtain a proper pattern for each temperature. From this, the behaviour of the wing pattern can be studied for the different temperatures.

The 1D-SAXS patterns obtained from the horizontal cuts of the 2D measurements at the height of the Yoneda feature were fitted to Beaucage's unified model[25,26]. This approach allows for multiple structural levels rather than just one type of scatterer. A traditional interpretation in terms of Guinier and Porod regimes would fail because these are only valid for restricted parts of the *q*-range; the Guinier method is generally only valid for $qR_g < 1$ (Ref.[27]), and the Porod method is only valid for the high-*q* slope. These limitations are corrected for in the unified model. Also, the traditional methods only account for one level of structural features, whilst the unified model can be extended to account for multiple levels of structural features, and it is therefore valid for the entire *q*-range. In the extended unified model, the total intensity is the sum of the contributions from each structural level[28,29]:

$$I(q) = \sum_{i=0}^{n-1} G_i \exp(-q^2R_{g,i}^2/3) + B_i \exp(-q^2R_{g,i+1}^2/3) \times \{[\mathrm{erf}(qR_{g,i}/\sqrt{6})]^3/q\}^{P_i}. \tag{10}$$

In adapting the unified model to the situation represented in the GISAXS patterns of YSZ sol-gels, we observe the following: The lowest number for n corresponds to the largest structural level, and by writing out Eq. (10) for $n = 2$, $R_{g,2}$ corresponds to a smaller structural level than has been observed here. If there were any scatterers in that size range, their signal would lie outside the q-range covered and hidden by the beamstop. Therefore we can set $R_{g,2} = 0$, and $\exp(-q^2R_{g,2}^2/3) = 1$ in this case. Since only a linear slope can be observed in the relevant range at the low-q end, we set $G_0 = 0$ and replace $B_0 \exp(-q^2R_{g,1}^2/3)\{[\mathrm{erf}(qR_{g,0}/\sqrt{6})]^3/q\}^{P_0}$ with $B_0' q^{-P_0}$. Therefore, for the q-range observed here, the unified model is given by Eq. (11), where the subscripts indicate which structural level it applies to:

$$\begin{aligned} I(q) = \quad & B_0' q^{-P_0} + S_1(q) \\ & \times \left(G_1 \exp(-q^2R_{g,1}^2/3) + B_1\{[\mathrm{erf}(qR_{g,1}/\sqrt{6})]^3/q\}^{P_1} \right) \\ & + C. \end{aligned} \quad (11)$$

The first term describes the low-q behaviour (level 0), with prefactor B_0', and where P_0 is the slope of this line when plotted on a log (I) *vs.* log (q) plot. The second term describes the next structural level (level 1): the first term within the parentheses is the Guinier term and the last term is the Porod term, with prefactors G_1 and B_1, respectively. $R_{g,1}$ is the median radius of gyration; it gives information about the size of the scattering particles at level 1. P_1 is the Porod slope for the same level, giving information about the roughness of the particle surfaces. C is a constant background contribution.

For most of the temperature range it is necessary to include a structure factor $S(q)$ to level 1 in Eq. (11), and the one used here is based on the Hosemann model for paracrystalline systems[30,31]. The semi-empirical function for $S(q)$ in Refs.[28,32], which describes damped spherical correlations of colloid particles was also considered, and was found to give worse results at high-q than the Hosemann model, which is given by (see, for example, Refs.[33,34])

$$S(q) = \frac{1 - \phi(q)^2}{1 - 2\phi(q)\cos(q\bar{a}) + \phi(q)^2}. \quad (12)$$

$\bar{a}$ is the average separation distance between neighbours, and $\phi(q)$ is the Fourier transform of the Gaussian distribution of first neighbours:

$$\phi(q) = e^{-w^2q^2}, \quad (13)$$

where we have used the substitution $w = \sigma/\sqrt{2}$ (σ is the standard deviation for the Gaussian distribution).

A constant fit parameter C was included to account for background scattering. For sample A, the value of C was successfully obtained from the fits for most of the temperature range. The value obtained for C was plotted as a function of T (in Fig.6), and it was found to follow a linear trend with a low slope. This fitted line was used for estimating $C(T)$ for sample B, where scattered intensity reaches to higher values of q and obscures the background, making a fit rather aribitrary. Thus it has been assumed that the slope of $C(T)$ is the same for both samples.

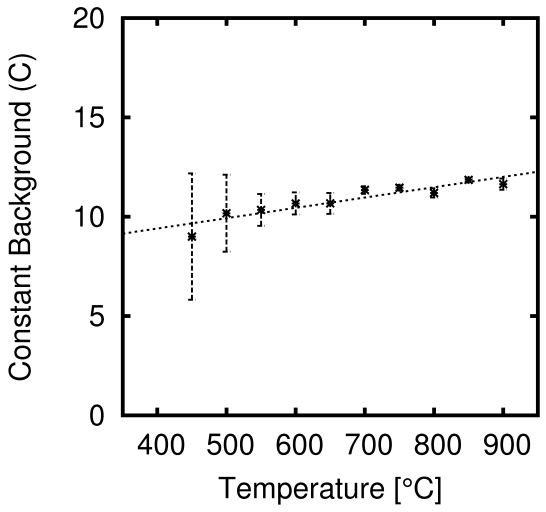

Fig. 6 Fitted value for C, for sample A. The straight line is described by $C(T) = 0.00519 \cdot T + 7.33$.

Table 2 Table summing up how the unified model [Eq. (11)] was used for sample B for the different temperature ranges.

Regime	Temperature °C	Fit range (q) nm^{-1}	$S(q)$	Background ($C(T)$)
1^{st}	400-550	0.027-1.38	1	$0.00519 \cdot T + 3.77$
2^{nd}	550-750	0.12-1.38	Eq. (12)	$0.00519 \cdot T + 3.77$
3^{rd}	750-1000	0.12-1.38	Eq. (12)	fitted

Eq. (11) was fitted to all measurements. Since the changes of the system are significant, the same model does not apply adequately to the whole experiment. Therefore, appropriate subsets for different (and overlapping) regimes are used (see Tab.2) instead of one unique model that would be overdetermined for part of the series of data sets. The overlap in regimes is to ensure continuity between the subsets. The reason for different fit ranges is that the beamstop covered a wider region of q for the second and third temperature regime. Moreover, including $S(q)$ as given by Eq. (12) for the first regime produced overdetermined fits. The constant background parameter C could be fitted for the third temperature regime because there is a sufficiently long flat region at high-q, and therefore C has been included as a fit parameter in this regime.

In order to test the different subsets, the normalised residuals of the two first subsets from the measured data were plotted

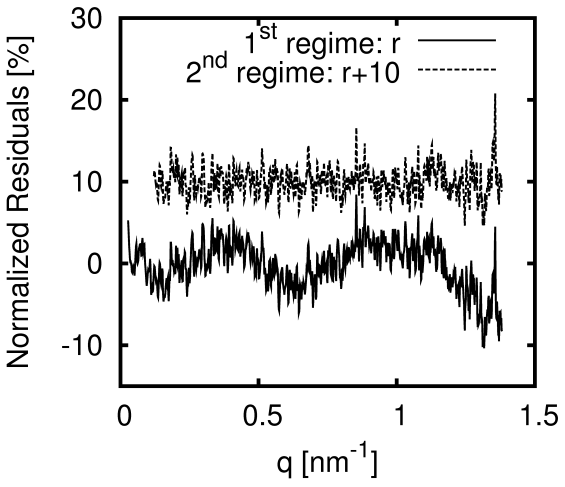

Fig. 7 Comparison of the first and second fit regime procedures, for the measurement taken at 550°C, using normalised residuals.

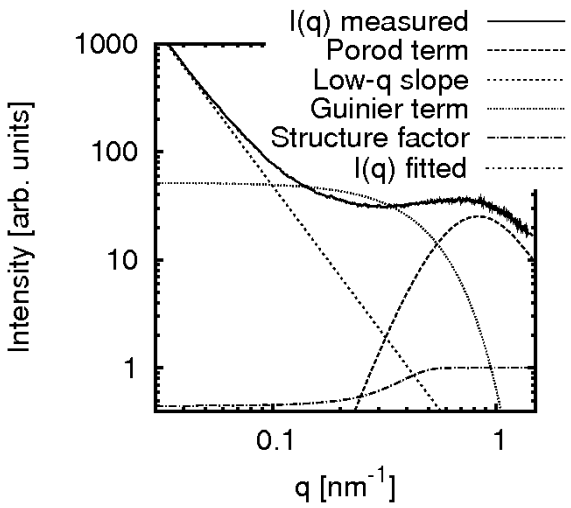

Fig. 8 Illustration on how the unified model [Eq. (11)] was fitted to the data taken at 550°C. Here the subset for the second fit regime was used.

at the overlap temperature 550°C; see Fig.7. From this figure it is clear that the second subset fits the data better, and this fit is shown in Fig.8.

Fig.9 shows the resulting radii of gyration $R_{g,1}$ (a), Porod slopes P_1 (b), and average distances between scattering objects $\bar{a}$ (c), for sample B. The increase in radius of gyration tells us that the size of the scattering particles increases as the sample is heated. The value of the Porod slope for this sample increases as the sample is heated, up to around -4 (at 850°C); this corresponds to the surface structure of the scattering objects to become smooth. The value of the Porod slope decreases again at the highest temperatures, to around -2.3 (at 1000°C), indicating a rougher surface structure once more. The discrepancy at 550°C is explained by the fact that the first fitting regime did not fit especially well (as shown in Fig.7).

The increase in the value for $\bar{a}$ means that the scattering particles are positioned further apart for higher temperatures. Since the particle size is also increasing, this suggests that the particles are undergoing Ostwald ripening.

The penetration depth, Λ, and also the film thickness decrease as the film is heated. In order to show how large the illuminated fraction of the film is, the film thickness, measured from ellipsometry, and Λ, estimated from Eq. (3), are plotted in Fig.10(a). Fig.10(b) is an estimate of the number of layers of particles within the penetration depth: $\Lambda/(2R_g)$.

In Fig.2, the appearance of small "wings" in the panel corresponding to the 550°C measurement, is characteristic of a 2D component in the scattering pattern. However, Fig.10 illustrates that the measured signal extends from a sufficient depth such that it might be expected to be three-dimensional. Therefore, we conclude that a layer of this 3D film has predomi-

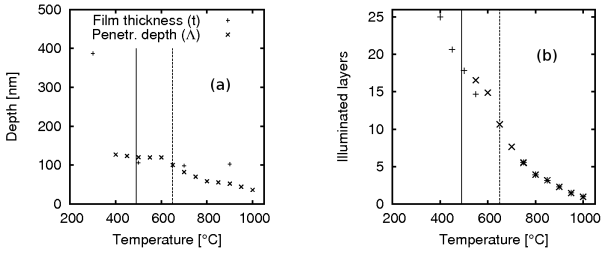

Fig. 10 (a) The theoretically calculated penetration depth Λ for sample B, and the film thickness t of a similarly prepared film measured by *ex-situ* ellipsometry. For the region $490°\text{C} \leq T \leq 650°\text{C}$ [vertical lines in both (a) and (b)], the penetration depth is larger than the film thickness. (b) Estimated number of illuminated layers of particles for the different temperatures: $\Lambda/(2R_g)$. The different symbols refer to the different fitting regimes.

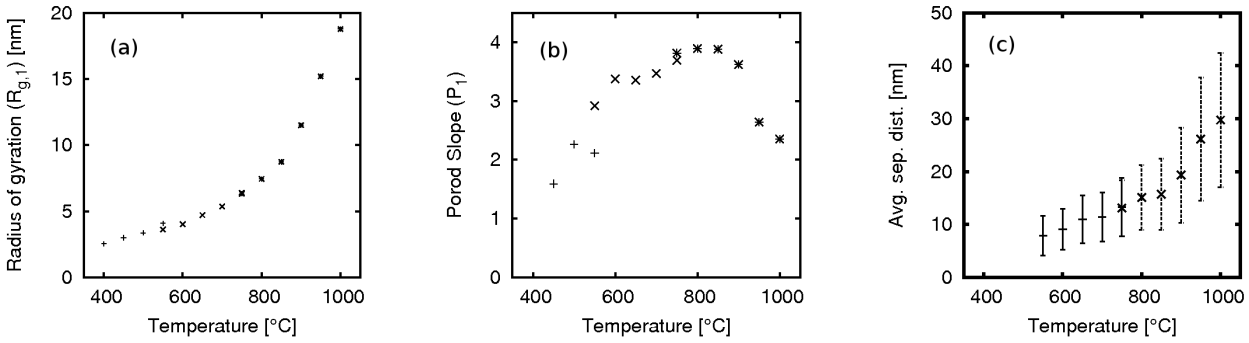

Fig. 9 The unified model applied to the heating run for sample B. The different symbols represent the different fitting regimes. (a) Radius of gyration ($R_{g,1}$). (b) Porod slope (P_1). (c) Average separation distance $\bar{a}$ between scattering objects [see Eq. (12)]. Note that the bars are not fitted error bars, but the result for the peak width: w in Eq. (13).

nantly 2D character.

As the sample is heated, the pattern changes, and for the 750°C measurement, a typical powder-like scattering pattern is obtained, which is an indication of a three-dimensional distribution of scattering centres. For this temperature, Λ is about 2/3 of the film thickness [$\Lambda/(2R_g) = 6$]. However, we cannot rule out that the pattern may also be a wing-type pattern where the particles have grown so large that the wings are disappearing out of the low-q window.

As the sample is heated further, it is observed that the scattering intensity has broadened in the y- and z directions. This is especially distinct for the 950°C measurement, and this is most likely due to a wing-pattern where the wings are disappearing at the low-q end. As already mentioned, this is typical for a two-dimensional distribution, which is to be expected considering that only 1 to 1.5 particle layers are within Λ at these high temperatures. Combining this finding with the result of the Porod analysis for the highest temperatures, where the particles were found to have rougher surfaces, it is a distinct possibility that only the particles in the topmost layer become rougher, whilst the particles further below in the film remain smooth.

These considerations lead us to an interpretation of the calcination mechanism as follows - Fig.11 represents the morphological evolution schematically. At 450°C, in the nucleation regime, the scattering particles are small and have rough surfaces, and they are randomly positioned in the sample. As the sample is heated, the particles undergo Ostwald ripening, and the particle surfaces become smoother, until the highest temperatures, where the particle surface, at least in the topmost layer, again becomes rougher. This roughening of the particle surfaces may be due to a growth instability.

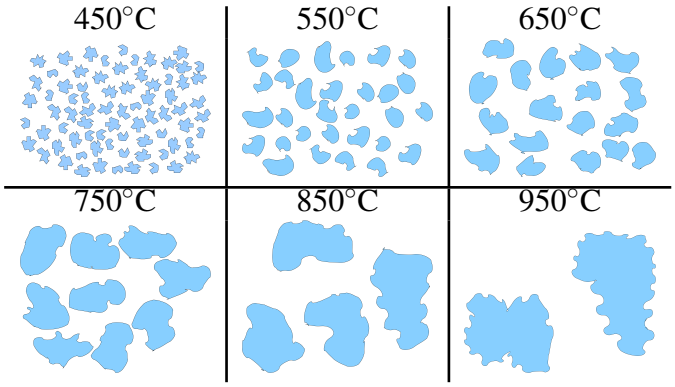

Fig. 11 Illustration of our interpretation of the available data, seen from above. The suggested morphological development during the heating programme is as follows: First, in the nucleation regime, the particles are small, irregular and randomly positioned. As the sample is heated, particles form larger, and fewer, particles where the average separation distance increases (Ostwald ripening). The medium between the particles would be air.

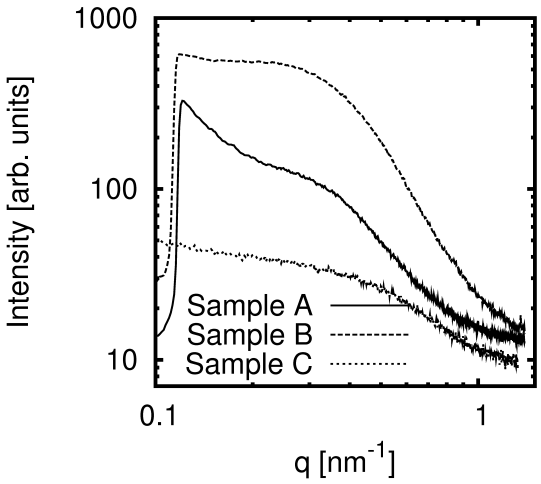

Fig. 12 Comparison of the 1D horizontal cuts for the samples containing different amounts of yttria; measured at 850°C.

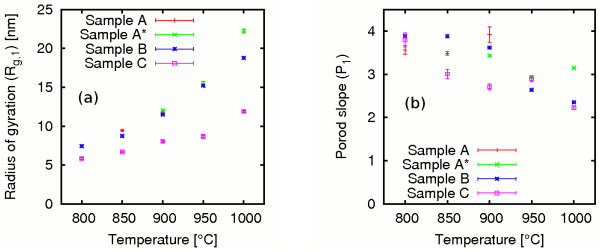

Fig. 13 Radius of gyration (a) and Porod slope (b) found for the different samples in the temperature range $(800-1000)$°C using the unified model [Eq. (11)]. For the sample marked with an asterisk (*), $S(q)=1$; otherwise, $S(q)$ from Eq. (12) is used. The error bars are the fitting uncertainties.

4.3 The role of the yttria concentration

Fig.12 shows the horizontal cuts for samples A, B, and C, taken at 850°C, in the same plot. Note that the intensity scaling is different between the samples and cannot be ascertained on an absolute scale because different fractions of the beam are captured by the sample. The position of the shoulder can, however, be compared; the position of the shoulder is very similar for samples A and B, whilst for sample C the shoulder is positioned at larger q.

The radius of gyration found using the unified model for the measurements taken at the temperatures $(800-1000)$°C is shown in Fig.13(a), and the Porod slope found is shown in Fig.13(b).

The radius of gyration found for samples A and B is practically the same (except at 1000°C) whilst for sample C it is noticeably smaller. For all of the samples, the radius of gyration increases with temperature, and thus the size of the scattering objects increases for all three samples.

The fitted Porod slope, as shown in Fig.13(b), is between -3.5 and -4 for both samplea A and B between 800°C and 900°C, *i.e.*, the surface structure of the scattering objects is smooth or nearly smooth for this temperature range. For sample A, the Porod slope changes to be around -3 at $(950-1000)$°C, whilst for sample B it changes even more, to around -2.3 (at 1000°C), indicating a rougher surface structure. For sample C the Porod slope decreases from -3.8 (800°C) to -2.6 (900°C), and therefore the surface structure of the particles changes from being smooth to becoming rougher at lower temperature than for the other samples.

These results were compared with XRD measurements on *ex-situ* samples which were annealed at 900°C. The peak widths were found to be wider at the higher yttria concentration, even wider than expected if only considering the results for different particle sizes found by GISAXS. This suggests that there is more chemical disorder in the crystalline lattice within the particles due to the onset of phase separation into yttria-richer and yttria-poorer regions, resulting in a range of lattice parameters within the YSZ structure.

5 Conclusions

Contrary to general perception, quantitative GISAXS data can be obtained under *in-situ* conditions where samples undergo chemical reactions or other processes which change their structure. We have demonstrated a procedure which allows us to compare data sets taken at different times during an *in-situ* experiment by using the relative positions of the Yoneda peak. This enables studies of surface processes such as catalysis, corrosion or layer-by-layer manufacturing of devices such as solar cells.

Sol-gel films have a complex, hierarchical structure which is difficult to describe with traditional SAXS analysis techniques such as Guinier or Porod analysis, which are based on a single structural level. Beaucage's unified model addresses this shortcoming and provides an opportunity to analyse complex scattering patterns of structures with multiple structural levels such as polymeric structures with embedded, agglomerated particles. Care has to be taken to ensure the model fit isn't overdetermined. This is achieved by limiting the number of structural levels to as few as possible while still matching the features of the scattering pattern. Therefore, we have adapted the unified model to the q-range covered in this experiment by limiting it to two distinct structural levels. At some temperatures, a structure factor is included representing the positional correlation of primary particles in the film.

The density and, hence, the penetration depth of x-rays in the film changes markedly during the initial stages of the sintering process due to the loss of organic precursor material. As

a result, the experiment is sensitive to several notional monolayers of particles at the lower temperatures, but only a single monolayer of agglomerates at the highest temperatures.

During the heating programme, both the values for scattering particle size and average separation distance were found to increase. This suggests that the particles are undergoing Ostwald ripening. The slope at high q indicates that the surface structure of the scattering objects is changing, to become smoother at first, then rougher again. This high-temperature transition to rougher particle surfaces depends on the yttria content: the more yttria, the earlier this transition happens. This suggests that particles segregate into regions of higher and lower yttria content at higher temperatures.

6 Acknowledgements

We would like to thank Matt Gunn, Dave Francis, John Parry, Les Dean, Dave Lewis and Clive Willson for designing and building the GISAXS furnace and the dip-coater, the late Tudor Jenkins for the ellipsometry result, Pascal Lenormand (Université Paul Sabatier, Toulouse) for useful information about XRR results on zirconia films, and Dag W. Breiby (Norges Teknisk-Naturvitenskapelige Universitet, Trondheim) for helpful discussions. We acknowledge funding from the Higher Education Funding Council for Wales through the Aberystwyth/Bangor Centre for Advanced Functional Materials and Devices and from the UK Engineering and Physical Sciences Research Council as well as beamtime at the BESSY storage ring at Helmholtz-Zentrum Berlin funded by the European Union (grant FP7/226716).

References

1 X. Ju, W. Feng, X. Zhang, V. Kittichungchit, T. Hori, H. Moritou, A. Fujii and M. Ozaki, *Solar Energy Materials and Solar Cells*, 2009, **93**, 1562–1567.

2 S. Alamri, *Solar Energy Materials and Solar Cells*, 2009, **93**, 1657–1662.

3 S. Phok, W. Zhao and R. Bhattacharya, *IEEE Transactions on Applied Superconductivity*, 2009, **19**, 3455–3458.

4 H.-T. Lim and A. V. Virkar, *Journal of Power Sources*, 2009, **192**, 267–278.

5 J. Müller, T. Böscke, U. Schröder, M. Reinicke, L. Oberbeck, D. Zhou, W. Weinreich, P. Kücher, M. Lemberger and L. Frey, *Microelectronic Engineering*, 2009, **86**, 1818–1821.

6 S. Teranishi, K. Kondo, M. Nishida, W. Kanematsu and T. Hibino, *Electrochemical and Solid-State Letters*, 2009, **12**, J73.

7 M. Sillassen, P. Eklund, M. Sridharan, N. Pryds, N. Bonanos and J. Bottiger, *Journal of Applied Physics*, 2009, **105**, 104907.

8 N. V. Russell, F. Wigley and J. Williamson, *Journal of Materials Science*, 2000, **35**, 2131–2138.

9 T. Barnardo, K. Hoydalsvik, R. Winter, C. M. Martin and G. F. Clark, *The Journal of Physical Chemistry C*, 2009, **113**, 10021–10028.

10 L. Landau and B. Levich, *Acta Physicochimica URSS*, 1942, **17**, 42–54.

11 J. R. Levine, J. B. Cohen, Y. W. Chung and P. Georgopoulos, *Journal of Applied Crystallography*, 1989, **22**, 528–532.

12 L. Parratt, *Physical Review*, 1954, **95**, 359–369.

13 A. Naudon and D. Thiaudiere, *Journal of Applied Crystallography*, 1997, **30**, 822–827.

14 M. Birkholz, *Thin Film Analysis by X-Ray Scattering*, Wiley-VCH, Weinheim, 2006.

15 J. Als-Nielsen and D. McMorrow, *Elements of Modern X-Ray Physics*, Wiley, Chichester, 2001.

16 R. Lazzari, *Journal of Applied Crystallography*, 2002, **35**, 406–421.

17 Y. Yoneda, *Physical Review*, 1963, **131**, 2010–2013.

18 O. J. Guentert, *Journal of Applied Physics*, 1965, **36**, 1361.

19 T. C. Huang, H. Toraya, T. N. Blanton and Y. Wu, *Journal of Applied Crystallography*, 1993, **26**, 180–184.

20 B. Lee, C.-T. Lo, S. Seifert and R. E. Winans, *Journal of Applied Crystallography*, 2006, **39**, 749–751.

21 P. Lenormand, A. Lecomte, D. Babonneau and A. Dauger, *Thin Solid Films*, 2006, **495**, 224–231.

22 T. Hanashima, *Numerical Tables of Anomalous Scattering Factors Calculated by the Cromer and Liberman's Method*, http://lipro.msl.titech.ac.jp/scatfac/scatfac.html.

23 J. W. Eaton, *Octave*, http://www.gnu.org/software/octave/.

24 K. Hoydalsvik, *PhD thesis*, Aberystwyth University, 2010.

25 G. Beaucage, *Journal of Applied Crystallography*, 1995, **28**, 717–728.

26 H. S. Jacobsen, H. A. Hansen, J. W. Andreasen, Q. Shi, A. Andreasen, R. Feidenhansl, M. M. Nielsen, K. Stå hl and T. Vegge, *Chemical Physics Letters*, 2007, **441**, 255–260.

27 A. Guinier and G. Fournet, *Small-Angle Scattering of X-Rays*, Wiley, New York, 1955.

28 G. Beaucage, *Journal of Non-Crystalline Solids*, 1994, **172-174**, 797–805.

29 K. Kravchyk, Y. Gomza, O. Pashkova, O. V'yunov, S. Nesin and A. Belous, *Journal of Non-Crystalline Solids*, 2009, **355**, 2557–2561.

30 R. Hosemann, *Acta Crystallographica*, 1951, **4**, 520–530.

31 R. Hosemann and S. N. Bagchi, *Acta Crystallographica*, 1952, **5**, 612–614.

32 S. Lenz, S. K. Nett, M. Memesa, R. F. Roskamp, A. Timmann, S. V. Roth, R. Berger and J. S. Gutmann, *Macromolecules*, 2010, **43**, 1108–1116.

33 B. K. Vainshtein, *Diffraction by Chain Molecules*, Elsevier, Amsterdam, 1966, p. 222.

34 G. Renaud, R. Lazzari and F. Leroy, *Surface Science Reports*, 2009, **64**, 255–380.